Automated layer segmentation of macular OCT images via Graph-Based SLIC Superpixels and Manifold Ranking Approach

Zhijun Gao[1,2] , Wei Bu [3, *], Yalin Zheng[4], and Xiangqian Wu[1]

[1]School of Computer Science and Technology, Harbin Institute of Technology, Harbin 150001, China
[2]College of Computer and Information Engineering, Heilongjiang University of Science and Technology, Harbin 150027, China
[3]Dept of Media Technology & Art, Harbin Institute of Technology, Harbin 150001, China
[4]Department of Eye and Vision Science, Institute of Ageing and Chronic Disease, University of Liverpool, UCD Building, Liverpool L69 3GA, UK

_____

ARTICLEINF

ABSTRACT

_____

Using the graph-based SLIC superpixels and manifold ranking technology, a novel automated intra-retinal layer segmentation method is proposed in this paper. Eleven boundaries of ten retinal layers in optical coherence tomography (OCT) images are exactly, fast and reliably quantified. Instead of considering the intensity or gradient features of the single-pixel in most existing segmentation methods, the proposed method focuses on the superpixels and the connected components-based image cues. The image is represented as some weighted graphs with superpixels or connected components as nodes. Each node is ranked with the gradient and spatial distance cues via graph-based Dijkstra's method or manifold ranking. So that it can effectively overcome speckle noise, organic texture and blood vessel artifacts issues. Segmentation is carried out in a three-stage scheme to extract eleven boundaries efficiently. The segmentation algorithm is validated on 51 OCT images in a database, and is compared with the manual tracings of two independent observers. It demonstrates promising results in term of the mean unsigned boundaries errors, the mean signed boundaries errors, and layers thickness errors.

_____

1. Introduction

Optical coherence tomography (OCT) is first introduced in 1991by Huang et al. [1], and it is a powerful, noninvasive and high resolution imaging modality used in the diagnosis and assessment of a variety of ocular diseases such as glaucoma and diabetic retinopathy[2-5]. Particularly, with the recent advancement of spectral domain optical coherence tomography (SD-OCT), higher resolution and more data have been acquired for clinical diagnosis [6]. But lacking fast and accurate quantification approach for more data, it is inconvenient for ophthalmologists or clinicians to directly diagnose for retinal diseases by calculating total retinal thickness, nerve fiber layer thickness, or outer plexiform layer thickness. Therefore, it becomes increasingly urgent to need an automated retinal layers segmentation approach in OCT images for clinical diagnosis or investigation.

Motivated by this need, the retinal layers segmentation algorithms based on the single pixel's intensity and gradient information have been mainly explored, and focused on the delineation of some intra-retinal layers during the last decade. Initially, the retinal layers segmentation mainly employed an image's peak intensity and gradient methods to segment only a few layers and extract to retinal boundaries, and investigated in [7, 8]. Then, active contour models have been built in retinal layers segmentation [9, 10]. Comparisons of initial methods, contour algorithms appeared good performance in resistance to 2D noise and in error, but has the limitation of selecting pre-determination of the initial seed points that are used in the convergence of the optimal path. Several recent researchers have explored the use of pattern recognition techniques for retinal layers segmentation. Mayer et al. employed a fuzzy C-means clustering technique to segment nerve fiber layer [11]. Kaji´c et al. proposed a accurate and robust segmentation method of intraretinal layers with a novel statistical model [12]. Vermeer et al. also introduced a six retinal layers segmentation method based on support vector machine (SVM) classifiers [13]. With the application of the graph cuts techniques for image segmentation, and graph cuts techniques emerged as one of the important retinal layers segmentation. Combining with spatial constraint information, Garvin et al. used graph cuts to extract nine boundaries [14]. Chiu et al. employed

_____

* Corresponding author. E-mail: buwei@hit.edu.cn

a dynamic programming techniques to extract eight retinal boundaries [15], and Yang et al. also used a dual-scale gradient information model to segment eight retinal layers[16].The graph search technique based on the single-pixel information can guarantee to find the global optimum, nevertheless it is relatively susceptible to speckle noise or artifact.

Recently, Kafieh et al. successfully used a coarse grained diffusion map method to segment eleven retinal layers and to determine the thickness map [17,18], the method like super-pixels based approaches can reduce the effects of unavoidable noise in OCT images, however, it needs indirectly detect boundaries by single pixel, and its time-consuming is relatively high in the coarse graining computation. Cha and Han also presented an intelligent tracking kernel method that could segment nine boundaries of eight retinal layers [19], but its processing time is also relatively long. Xinjian Chen and Fei Shi et al. successfully proposed a multi-resolution graph search based surface detection method to automatically segment the retinal layers in 3-D OCT data with serous retinal pigment epithelial detachments [20].

Most existing retinal layers segmentation algorithms mainly focus on the single pixel or region based on its intensity or gradient within a local context, whereas there is no a algorithm focuses on the whole edge-based image cues to automatically segment the retinal layers. Besides, it is inevitable that some intrinsic speckle noise, organic texture and blood vessel artifacts make difficult to exactly segment retinal layers.
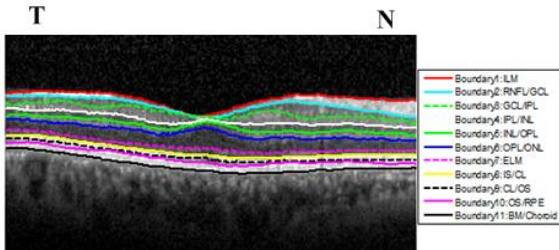
Fig.1. Illustrates eleven intra-retinal boundaries from top to bottom: boundary 1 ILM, boundary 2 NFL/GCL, boundary 3 GCL / IPL, boundary 4 IPL/INL, boundary 5 INL/OPL, boundary 6 OPL/ONL, boundary 7 ELM, boundary 8 IS/CL, boundary 9 CL/OS, boundary 10 OS/RPE, and boundary 11 BM/Choroid. (N: nasal, T: temporal).

In this work, inspired by superpixels, a novel three-stage using graph-based SLIC superpixels and manifold ranking approach is focused on intra-retinal layer segmentation of OCT images due to its eleven intra-retinal boundaries mainly correspond to high, middle or low contrast in pixels intensity, positive or negative vertical gradient values, and their spatial relationship between intra-retinal boundaries. Fig.1 illustrates eleven intra-retinal boundaries we desired to find in macular spectral-domain OCT images. It is relative to single-pixel, the proposed approach is based on the superpixels and connected components designated as nodes, making it able to well avoid the

intrinsic speckle noise, and to the possible presence of organic texture and blood vessel artifacts. The research demonstrates that such a proposed approach is able to automatically segment eleven boundaries of ten retinal layers in OCT images, and improve the accuracy, efficiency, and robustness of retinal layers segmentation.

In summary, our main contributions are as follows:

(a) Application of the superpixels and connected component, it can well avoid some disturbs from the intrinsic speckle noise and organic texture artifacts, and exactly detect boundary ILM and boundary IS/CL.

(b) Application of the manifold ranking and connected component, it can well overcome discontinuity from the intrinsic speckle noise and blood vessel artifacts, and exactly detect the other nine boundaries.

The rest of this paper is organized as follows, In Section 2 briefly introduces SLIC superpixels, manifold ranking method and the construction of the weighted graph, and describes the proposed intra-retinal layers segmentation algorithm via graph-based SLIC superpixels and manifold ranking technology in detail. The experiments and results are presented in Section 3. Finally, Section 4 concludes the paper.

2. Material and Methods

2.1.SLIC Superpixels and Manifold Ranking

Based on k-means clustering, Radhakrishna Achanta and Appu Shaji et al. successfully proposed a simple linear iterative clustering (SLIC) method for generating superpixels, which has been shown to outperform existing superpixel methods in image boundaries, memory efficiency, speed, and their impact on segmentation performance [21]. And the proposed method has achieved great success on image segmentation [22].

Zhou et al. successfully proposed a manifold ranking method, which exploits the intrinsic manifold structure of data for labeled graph [23]. Essentially, manifold ranking can be viewed as an one-class classification problem [24], that is, only positive examples or negative examples are required. Given a dataset $X = \{x_1, x_2, \cdots, x_n\} \in \mathbb{R}^{m*n}$, some data points are labeled queries that are assign a positive ranking score (such as 1), and zero to the remaining points. Let a ranking function $f : X \to R^n$, namely, a weighted network is form on the dataset, then, all points repeatedly spread their ranking score to their nearby neighbors via the weighted network, finally, all points except queries are ranked according to their final ranking scores when a global stable state is achieved. In order to conveniently compute the optimal ranking of queries, a graph $G=(V, E)$ is defined for the dataset, where the nodes V are the dataset X and the edges E are weighted by an affinity

matrix $W=[w_{ij}]_{n \times n}$, thereby, the degree matrix D is equal to $diag\{d_{11}, d_{22}, ..., d_{nn}\}$, where $d_{ii} = \sum_j w_{ij}$. Then, similar to the PageRank and spectral clustering algorithms [25, 26], the optimal ranking of queries can be obtained by solving the following optimization problem:

$$f^* = \arg\min_f \frac{1}{2}(\sum_{i,j=1}^{n} w_{ij} \| \frac{f_i}{\sqrt{d_{ii}}} - \frac{f_j}{\sqrt{d_{jj}}} \|^2 + \mu \sum_{i=1}^{n} \|f_i - y_i\|),$$

(1)

Where the first and the second term are respectively the smoothness constraint and the fitting constraint whose balance can be controlled by the parameter μ. Namely, for a good ranking function, the first term should not change too much between nearby points and the second term should not differ too much from the initial query assignment. Certainly, the optimal solution could be conveniently computed by setting the derivative of the above function to be zero, and the optimal resulted ranking function can be written as Eq. 2 by using the unnormalized Laplacian matrix. The Eq. 2 has achieved great success on image saliency detection [27].

$$f^* = (D - \theta W)^{-1} y,$$

(2)

2.2. Weighted Graph Construction

A weighted graph $G=(V,E,W)$ is constructed to represent OCT image, and exploit the gradient information and the spatial relationship, where V denotes a set of nodes, E denotes a set of undirected edges and W is defined to the affinity matrix that represents the weights of the edges between two arbitrary nodes. In this work, each node is a superpixel generated by the SLIC algorithm, and is only connected to those nodes neighboring it (See Fig.2a), or a part of connected component (a true or false boundary) generated by the classic canny edge detection [28], and is not only connected to those nodes neighboring it, but also connected to the nodes with its neighboring node (See Fig.2b). By extending the scope of node connection, so that neighboring nodes are likely to take on similar appearance, and we effectively utilize local smoothness cues. Besides, we assume that it is necessary condition of these adjacent nodes if their corresponding gradient value is the same positive or negative in the same boundary. This gradient constraint significantly improves the performance of the proposed method as it effectively avoid the connection for some neighboring nodes, thereby improving the ranking results of the boundary detection. It is clear that the weighted graph G is a sparse. That is, most elements of the affinity matrix W are zero, which is also able to upgrade compute rate by sparse matrix. In this work, W is defined by Eq.3. and Eq.4, since eleven intra-retinal boundaries of the OCT image mainly correspond to low, middle or high contrast in pixels intensity, positive or negative vertical gradient values, and their spatial

relationship between intra-retinal boundaries.
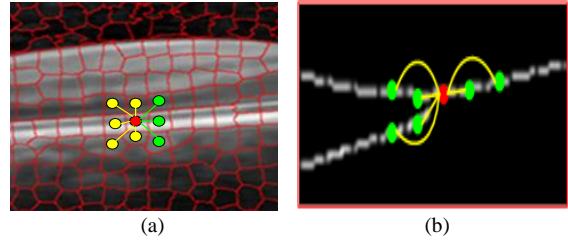
(a)   (b)
Fig.2. Our graph model. (a) Graph model based on the SLIC superpixels. (b) Graph model based on the connected components.

where $F_i = (\tilde{f}_i, \tilde{g}_i)$ or ($\tilde{g}_i$, $\bar{y}_i$), $\tilde{f}_i$ and $\tilde{g}_i$ denote respectively the sum of the connected component (superpixel) corresponding to a node in the intensity and gradient value of the pixels, $\bar{y}_i$ denotes the mean of the connected component (superpixel) corresponding to a node in the row-coordinate of the pixels, X_i and Y_i denote respectively the start and end vertex of connected component (superpixel) corresponding to a node in the coordinate of the pixels, for i, $j=1,2,...,|V|$. This matrix naturally captures texture information and spatial relationship information. Namely, the affinity value $w(i, j)$ between nodes is increased when their intensity value is close or spatial distance is decreased, So that $w(i, j)$ can present texture information, and constraints spatial relationship well.

$$w(i, j) = \exp(\frac{\|F_i - F_j\|_2^2}{-2\delta^2}) * sgn(X_i, Y_j)$$

(3)

$$sgn(X_i, Y_j) = \begin{cases} 1 & e_1 < X_i - Y_j < e_2 \\ 0 & othersize \end{cases}$$

(4)

2.3. Three-Stage Boundaries Detection

In this section, the proposed three-stage scheme is detailed for OCT boundaries detection using graph-based SLIC superpixels and manifold ranking method with texture information, the spatial relationship.

2.3.1 Detect the ILM and IS/CL boundaries

Among eleven boundaries in an SDOCT retinal image, the ILM and IS/CL are the two most prominent boundaries due to their high contrast in pixel intensity, so our algorithm firstly detects the ILM and IS/CL boundaries as follows. Unfortunately, it is inevitable that some intrinsic speckle noise and organic texture artifacts make difficult to exactly detect their end points and them, for example, in the upper left and upper right corner of Fig.3a, there exist two organic texture artifacts.

In order to simultaneously reduce noise and preserve edges, on the one hand, a classic and effective median filter is applied for OCT images. Consequently, the high contrast connected components can be detected by a classic canny edge detector with high-valued threshold (0.5*automated threshold), which could remove the false boundaries, and to highlight the significant boundaries as shown

in Fig.3b. On the other hand, for the possible presence of organic texture artifacts, whose connected component obviously joints with ILM boundary in the upper left corner of Fig.3b. Firstly, superpixels are segmented by SLIC superfixels approach for filtered OCT image as shown in Fig.3c. Next, a weighted graph $G=(V,E,W)$ is constructed by the superfixels，and its affinity matrix W is computed by Eq.3 and Eq.4, where $F_i = (\tilde{f}_i, \tilde{g}_i)$. Then, our algorithm utilizes Dijkstra's method to successively find the two lowest-weighted path initialized at the four vertices of the graph, whose gradient value are maximum at the two left and two right vertices of the graph. Fig.3d shows the two paths that can well avoid the distraction from intrinsic speckle noise around boundary ILM and boundary IS/CL. We perform morphological closing on the two paths with a disk structuring element, and Fig.3e shows the fusion image by the two processed paths and the main connected components (white) around the ILM (green) and IS/CL (purple) boundaries, on the one hand, the connected components of organic texture artifacts are removed, on the other hand, the own regions of boundary ILM and boundary IS/CL are exactly located. Finally, the connected components of both ILM and IS/CL boundaries are flawlessly detected by the uppermost connected components from the processed paths, in order to show so much smooth boundary, respectively, the results are enhanced by twenty and twelve orders polynomial smoothing as shown in Fig.3f. So that the other connected components can be restricted to successively two smaller search areas as shown in Fig. 4a, respectively, followed by the simultaneous detection of boundaries 7, 9, 10, 11 below boundary 8, and boundaries 2, 3, 4, 5, 6 between boundaries 1 and 8.
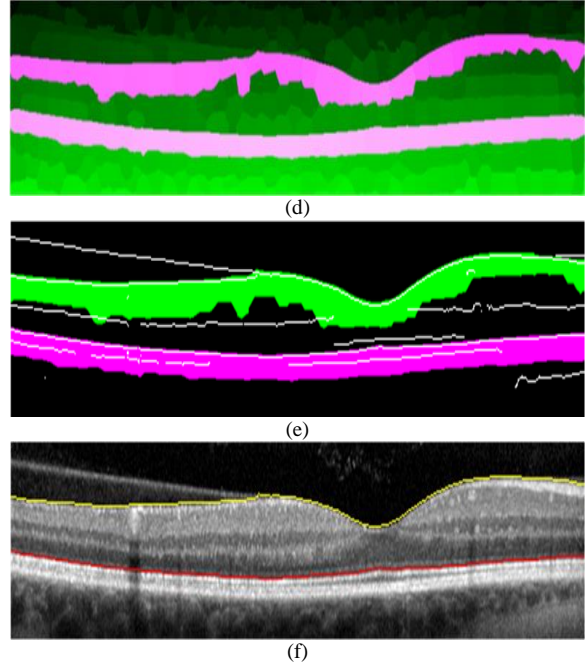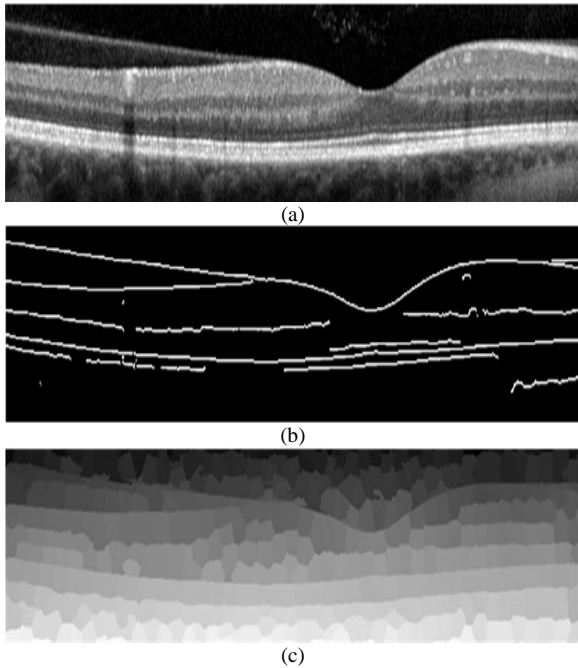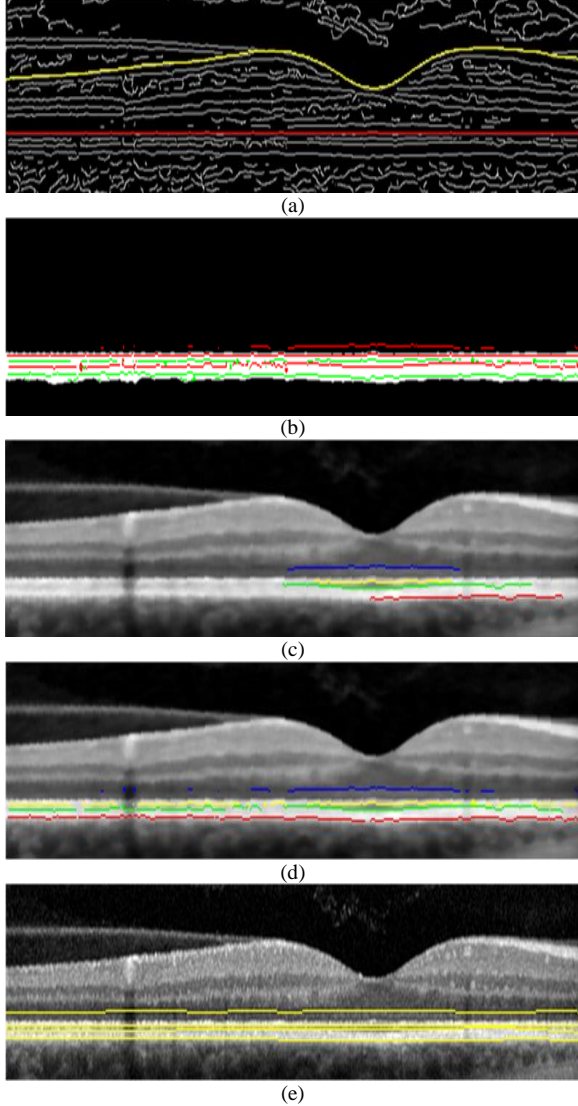

Fig. 3. Images show how the ILM and IS/CL boundaries are found via the graph-based SLIC superfixels and manifold ranking approach. (a)Original OCT image. (b) High contrast connected components. (c) Result of applying SLIC superpixels. (d) Result (purple) of applying by Dijkstra's method for Fig.3c. (e) Fusion image by the processed paths and the main connected components (white) around the ILM (green) and IS/CL (purple)boundaries (f) Result of the ILM (yellow) and IS/CL (red) boundaries after smoothing.

2.3.2. Detect the ELM and boundaries below IS/CL

Based on the detection of boundaries 1st and 8th, firstly, the OCT image is aligned according to the 8th boundary. Which served multiple purposes: on the one hand, to allow for smaller image sizes in the segmentation step and provide for a more consistent shape for segmentation purposes as shown in Fig. 4a, on the other hand, to make visualization easier and conform to clinical practice[14]. Fig. 4a shows that the low and middle contrast connected components can be also detected in the aligned image by a classic canny edge detector with low-valued threshold (0.05*automated threshold), which detects the significant boundaries and preserves other potential boundaries as well. Fig. 4b shows that the second aligned superfixels path and above it can almost contain all the connected components of the boundaries7, 9,10, and 11.

Next, respectively, we construct four weighted subgraphs $G_7=(V_7,E_7,W_7)$ by the connected components, whose vertical gradient values are positive in a vertical search area between d_{71} and d_{72} pixels above boundary 8, $G_9=(V_9,E_9,W_9)$ by the connected components, whose vertical gradient values are negative in a vertical search area between d_{91} and d_{92} pixels below boundary 8, $G_{10}=(V_{10},E_{10},W_{10})$ by the connected components, whose vertical gradient values are positive in a vertical search area between d_{101} and d_{102} pixels below boundary 8, and $G_{11}=(V_{11},E_{11},W_{11})$ by the connected components,

whose vertical gradient values are negative in a vertical search area between d_{111} and d_{112} pixels below boundary 8, and their affinity matrices W_7, W_9, W_{10}, and W_{11} are computed successively by Eq.5, Eq.3, Eq.6, and Eq.7, where $F_i = (\tilde{g}_i, \overline{y}_i)$ in Eq.3, whose purpose is able to constraint spatial relationship between nodes well.

(a)

(b)

(c)

(d)

(e)

Fig. 4. Images show how the ELM and boundaries below IS/CL are found via our proposed approach. (a) The main connected components.(b) Fusion image by the segmented superpixels (white), the main positive(red) and negative (green) connected components around the ELM boundary. (c) Automatically selected queries of the boundary 7 ELM (a blue connected component), boundary 9 CL/OS (a yellow connected component), boundary 10 OS/RPE(a green connected component), boundary 11 BM/Choroid (a red connected component). (d) Result of the connected components of the boundary 7 ELM (blue), boundary 9 CL/OS (yellow), boundary 10 OS/RPE(green), boundary 11 BM/Choroid (red) with manifold ranking. (e) Result (yellow) of boundaries 7, 9, 10 and 11 after smoothing.

$$W_k(i, j)= W(i, j).*sgn(W_G(i)).*sgn(W_R(i)), \quad (5)$$

Where $W_G(i)= g_i$, $W_R(i)= \overline{y}_i$, $i=1, 2, \ldots, |V|$, and $k=2,3,4,5,6,7,9,10,$ and11.

$$sgn(W_G(i)) = \begin{cases} 1 & s_k * W_G(i) > 0 \\ 0 & otherwise \end{cases} \quad (6)$$

$$sgn(W_R(i)) = \begin{cases} 1 & bd_{k1}(\overline{x}_i) + d_{k1} \le W_R(i) \le bd_{k2}(\overline{x}_i) + d_{k2} \\ 0 & otherwise \end{cases} \quad (7)$$

Where s_7 and s_{10} are equal to 1 due to vertical gradient values of the boundaries 7and 10 are positive, and conversely s_9 and s_{11} are equal to -1 in Eq.6. The $\overline{x}_i$ denotes the mean of connected component corresponding to a node in the column-coordinate of the pixels, for k=7, 9, 10 and 11, let $bd_{k1}(\overline{x}_i)$ and $bd_{k2}(\overline{x}_i)$ correspond to the row-coordinate of boundary 8 when their column-coordinates are $\overline{x}_i$, and d_{71}=-10, d_{72}=-1, d_{91}=1, d_{92}=10, d_{101}=3, d_{102}=20, d_{111}=10, d_{112}=25 in Eq.7. So that sgn(W_G)can represent gradient information, and $sgn(W_R)$ constraints spatial relationship well.

Then, all nodes are respectively ranked according to their final ranking scores by Eq.2, where queries are respectively selected one node from the highest gradient value of the nodes for the 7th(blue) and 10th(green) boundaries, and the lowest gradient value of the nodes for the 9th (yellow) and 11th (red) boundaries as shown in Fig. 4c, where the four connected components are successively belong to queries of the boundaries 7, 9, 10 and 11 from up to down. Fig. 4d shows the result of the connected components with manifold ranking, which could not only effectively reject some connected components of the other salient noise boundaries, but also well reserve the connected components of the four boundaries, relative to the Fig. 4 a. Particularly, such as the right end of the boundary 7 in Fig. 4d, which can not be detected due to its low or middle contrast in pixel intensity. Nevertheless, in order to the next smoothing step, the right end of the boundary 7 is defined to the mean vertical distance of the connected components between the detected boundary 7 and 8.

Finally, in order to show so much smooth boundary, respectively, the results are enhanced by twenty, six, six and six orders polynomial smoothing as shown in Fig. 4e.

2.3.3.Detect the boundaries between ILM and ELM

Based on the above results, in order to detect accurately the boundaries 2, 3, 4, 5, and 6 as follows. Similarly, a weighted subgraph $G_5=(V_5,E_5,W_5)$ is constructed by the connected components, whose vertical gradient values are positive in a vertical search area between d_{51} pixels below boundary 1 and d_{52} pixels above boundary 7, and its affinity matrix W_5 is computed by Eq.5, where $F_i = (\tilde{g}_i, \overline{y}_i)$ in Eq.3, and s_5=1 for Eq.6. Let dy_{ij} denote the mean distance of the row-coordinate of the ith boundary and the jth boundary, so d_{51} and d_{52} are respectively equal to 0.1*dy_{17} and -0.3*dy_{17} for Eq.7, that $sgn(W_R)$ can constraint spatial relationship well. Then, all nodes are respectively ranked according to their final ranking scores by Eq.2, where queries (red) are

respectively selected two nodes from the highest gradient value of the nodes for the left and right parts of the 5th boundary as shown in Fig.5a, which could avoid no connectivity of the boundary due to its low contrast in pixel intensity around macular fovea. Fig. 5b shows the result (red) of the connected components with manifold ranking, which could not only effectively reject some connected components of the other salient noise boundaries, but also well reserve the connected components for the 5th boundary, relative to Fig.4a. Certainly, in Fig.5b, the two ends of the boundary 5 might not be also detected due to its low or middle contrast in pixel intensity, and they would be also defined to the mean vertical distance of the connected components between the detected boundary 5 and 7, so that conduces to the next smoothing step. Finally, the result (red) is enhanced by sixteen orders polynomial smoothing as shown in Fig. 5c.

(f)
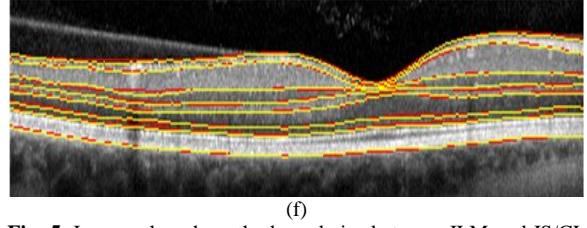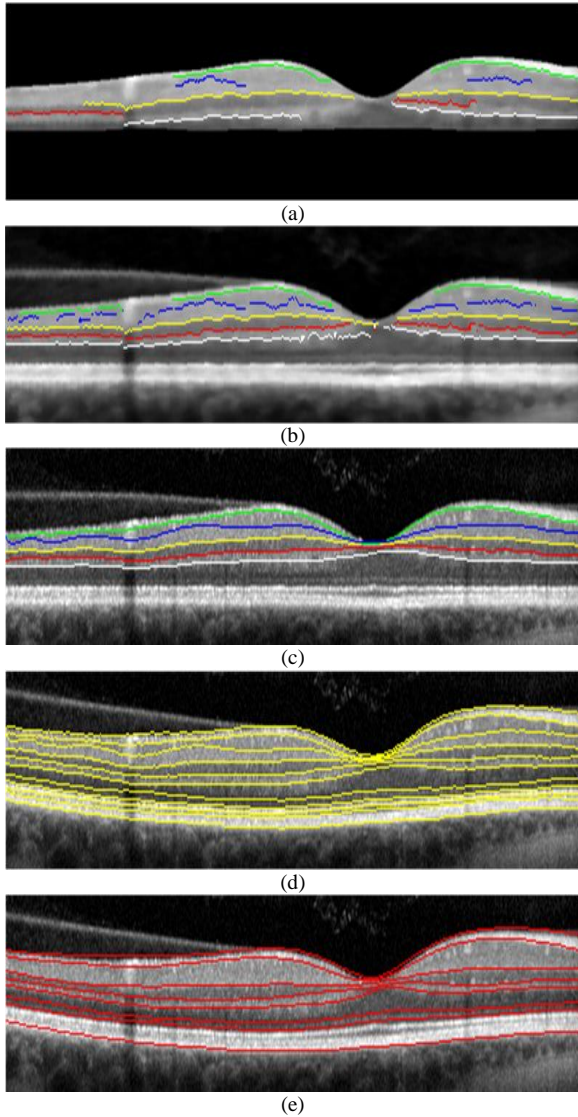
Fig. 5. Images show how the boundaries between ILM and IS/CL are found using our proposed approach. (a) Automatically selected queries of the boundary 2 NFL/GCL (two green connected components), boundary 3 GCL/IPL (two blue connected components), boundary 4 IPL/INL(two yellow connected components), boundary 5 INL/OPL(two red connected components), and boundary 6 OPL/ONL(two white connected components), successively. (b) Result of the connected components of the boundary 2 (green), boundary 3 (blue), boundary 4 (yellow), boundary 5 (red), and boundary 6 (white), successively. (c) Result of boundary 2(green), boundary 3 (blue), boundary 4 (yellow), boundary 5 (red), and boundary 6 (white) after final ranking. (d) Final segmentation for the original image after smoothing. (e) Original image showing referenced standard. (f) Comparison of computer-segmentation (yellow) and independent standard (red).

(a)

(b)

(c)

(d)

(e)

For the detection of the boundaries 4, and 6, on the basis of the detection of the boundaries 1, 5, and 7, firstly, we construct two affinity subgraphs $G_4=(V_4,E_4,W_4)$ by the connected components, whose vertical gradient values are also negative in a vertical search area between d_{41} pixels below boundary 1and d_{42} pixels above boundary 5, and $G_6=(V_6,E_6,W_6)$ by the connected components, whose vertical gradient values are negative in a vertical search area between d_{61} pixels below boundary 5 and d_{62} pixels above boundary 7. Successively, and compute their weight matrices W_4 and W_6 by Eq.5, where s_4 and s_6 are all equal to -1 for Eq.6 since these boundaries correspond to connected components whose gradient value of the pixels should be negative. For Eq.7, both $bd_{41}$and bd_{42} all correspond to the boundary 5, both $bd_{61}$and bd_{62} respectively correspond to the boundary 5 and boundary 7, d_{41} is equal to $-0.25*dy_{15}$, and d_{42} is equal to -1, d_{61} is equal to 1, and d_{62} is equal to -1, so that $sgn(W_R)$ can constraint spatial relationship well. Then, all nodes are respectively ranked according to their final ranking scores by Eq.2, where queries (yellow and white) are respectively selected two nodes from the lowest gradient value of the nodes for the left and right parts of the boundaries 4 and 6 as shown in Fig. 5a. Fig. 5b shows the results (yellow and white) of the connected components with manifold ranking, which could not only effectively reject some connected components of the other salient noise boundaries, but also well reserve the connected components for the 4th and 6th boundaries, relative to Fig.4a. Certainly, if the two ends of the boundaries 4 or 6 might not be also detected due to its low or middle contrast in pixel intensity, then they would be also respectively defined to the mean vertical distance of the connected components between the detected boundaries 4 and 5, or 6 and 5, so that conduces to the next smoothing step. Finally, the results (yellow and white) are respectively

enhanced by sixteen orders polynomial smoothing as shown in Fig. 5c.

For the detection of the boundary 2, on the basis of the detection of the boundaries 1, and 4, firstly, an affinity subgraph $G_2=(V_2,E_2,W_2)$ by the connected components, whose vertical gradient values are negative in a vertical search area between d_{21} pixels below boundary 1and d_{22} pixels above boundary 4. Its affinity matrix W_2 is computed by Eq.5, where s_2 is all equal to -1 for Eq.6 since its boundary corresponds to connected components whose gradient value of the pixels should be negative. For Eq.7, both $bd_{21}$and bd_{22} respectively correspond to the boundaries 1 and 4, d_{21} is equal to 1, and d_{22} is equal to -0.3*dy_{14}, so that $sgn(W_R)$ can constraint spatial relationship well. Then, all nodes are respectively ranked according to their final ranking scores by Eq.2, where queries (green) are respectively selected two nodes from the lowest gradient value of the nodes for the left and right parts of the boundary 2 as shown in Fig. 5a. Fig. 5b shows the result (green) of the connected components with manifold ranking, which could not only effectively reject some connected components of the other salient noise boundaries, but also well reserve the regular connected components for the 2th boundary. Certainly, the two ends of the boundary 2 might not be also detected due to its low or middle contrast in pixel intensity, and they would be also respectively defined to the mean and max vertical distance of the connected components between the detected boundaries 1 and 2, so that conduces to the next smoothing step. Finally, the result (green) is enhanced by twenty orders polynomial smoothing as shown in Fig.5c.

Based on boundaries 2 and 4, finally, for the detection of the boundary 3, similarly, a affinity weighted subgraph $G_3=(V_3,E_3,W_3)$ is constructed by the connected components, whose vertical gradient values are positive in a vertical search area between d_{31} pixels below boundary 2 and d_{32} pixels above boundary 4, and its weight matrix W_3 is computed by Eq.5,where s_3 is equal to 1 for Eq.6 since the boundary 3 correspond to connected components whose gradient value of the pixels should be positive. For Eq.7, $bd_{31}$and bd_{32} respectively correspond to the boundary 2 and the boundary 4, d_{31} and d_{32} are respectively equal to 1 and -1, so that $sgn(W_R)$ can constraint spatial relationship well. Then, all nodes are respectively ranked according to their final ranking scores by Eq.2, where queries (blue) are respectively selected two nodes from the highest gradient value of the nodes for the left and right parts of the boundary 3 as shown in Fig. 5a. Fig.5b shows the result (blue) of the connected components with manifold ranking, which could not only effectively reject some connected components of the other salient noise boundaries, but also well reserve the connected components for the 3th boundary. Certainly, the two ends of the boundary 3 might not be also detected due to its low or middle contrast in pixel

intensity, and they would also respectively defined to the mean and max vertical distance of the connected components between the detected boundaries 2 and 3, so that conduces to the next smoothing step. Finally, the result (blue) is enhanced by sixteen orders polynomial smoothing as shown in Fig. 5c.

Finally, for the boundaries 2, 3, 4, 5 and 6, Fig. 5 b shows the whole results of the connected components with manifold ranking approach, which could not only effectively reject some connected components of the other salient noise boundaries, but also well reserve the connected components for these boundaries, relative to Fig.4a. Fig.5d shows the extracted results of the eleven boundaries. Fig.5e shows the reference standard for original image. Fig.5f shows their comparison of computer-segmentation (yellow) and reference standard (red), demonstrates that they are almost identical, and our proposed approach can well avoid the intrinsic speckle noise, and the possible presence of blood vessel and organic texture artifacts.

The main steps of the proposed lay segmentation algorithm are summarized in Algorithm 1.

_____

Algorithm 1

_____

Input: An OCT image and required parameters
Step1. Detect the ILM and IS/CL boundaries.
   Step 1.1 Enhance the input image by median filter.
   Step 1.2 Detect the high contrast connected components by canny edge detector for filtered image.
   Step 1.3 Segment the filtered image into superpixels, construct a graph G with superpixels as nodes, and compute its affinity matrix W by Eq3, utlize Dijkstra's method to find the two lowest weighted paths, and perform morphological closing on the two paths with a disk structuring element.
   Step 1.4 Detect the main connected components of the boundaries 1 and 8 by the results of step 1.2 and 1.3, and obtain boundaries 1 and 8 by fitting.
Step 2. Detect the ELM and boundaries below IS/CL
   Step 2.1 Align the filtered image according to the boundary 8.
   Step 2.2 Detect the low and middle contrast components by canny edge detector for aligned image.
   Step 2.3 Construct four graphs G_7 , G_9 , G_{10}, and G_{11} with connected components as nodes, successively, and compute their affinity matrix W_7 , W_9 , W_{10} and W_{11} by Eq5, utlize manifold ranking method to detect their own connected components, and obtain boundaries 7, 9, 10 and 11 by fitting.
Step 3. Detect the boundaries between ILM and ELM
   Step 3.1 Construct graph G_5 with connected components as nodes on the basis of the boundaries 1 and 7, and compute its affinity matrix W by Eq5, utlize manifold ranking method to detect connected components, and obtain boundary 5 by fitting.
   Step 3.2 Construct two graphs G_4 and G_6 with connected components as nodes on the basis of the boundaries 1, 5 and 7, respectively, and compute their affinity matrix W_4 and W_6 by Eq5, utlize manifold ranking method to detect their own connected components, and obtain boundaries 4 and 6 by fitting.
   Step 3.3 Construct graph G_2 with connected components as nodes on the basis of the boundaries 1 and 4, and compute its affinity matrix W_2 by Eq5, utlize manifold ranking method to detect connected components, and obtain boundary 2 by fitting.
   Step 3.4 Construct graph G_3 with connected components as nodes on the basis of the boundaries 2 and 4, and compute its affinity matrix W_3 by Eq5, utlize manifold ranking method to detect connected components, and obtain boundary 3 by fitting.
Output: the lay segmentation image.

_____

3. Experiments and Results

The proposed algorithm was evaluated against the manual tracings of two independent observers (retinal specialists) with the use of a computer-aided manual segmentation procedure on one 2D-labeled macular OCT dataset (Cirrus, Zeiss Meditec). The dataset contains 51 slices with the ground truth of marked boundaries, and is from different human eye, each image had x, y dimensions of 2×6 mm^2, 496×1024 pixels sized 4.03×5.86 μm^2. The two independent observers did not attempt to trace some boundaries that they considered invisible, such as the GCL/IPL, CL/OS and OS/BM. The proposed algorithm was implemented in Matlab, the dataset was processed by a personal computer (CPU:Core 2, 2.53GHz, RAM:4 GB). For comparisons, the mean signed and unsigned border positioning differences for the ILM, NFL/GCL, IPL/INL, INL/OPL, OPL/INL, ELM, IS/CL and BM/Choroid boundaries were computed. In addition, for the purpose of the clinical and medical analysis, the mean thickness of each layer was respectively computed by the proposed algorithm and each observer, where the algorithm and each observer all excluded the fovea area, namely, not computed the middle 30 pixels, since it is invisible for the some boundaries around fovea area. The two observers computed the mean thicknesses that were used as a reference standard.

The proposed approach successfully detected all eleven intra-retinal boundaries in the datasets of 51 OCT images. It took about 9.6 seconds in Matlab for the full ten layers segmentation for each 2D slice in normal segmentation processing mode. The mean unsigned and signed border positioning differences for the main boundaries are presented in Tabel 1 as follows. The unsigned border positioning mean errors between the proposed algorithm and the reference standard, whose overall errors 0.94 pixels was less than 1 pixel, ILM errors 0.66 pixels and IS/CL errors 0.55 pixels were far less than 1 pixel, NFL/GCL errors 1.27 pixels was maximum error, but were respectively smaller than those computed between the observers. The signed border positioning errors between the proposed algorithm and the reference standard was 0.30 pixel, and was approximate to those computed between the observers, ILM errors 0.13 pixels and IS/CL errors 0.23 pixels were far less than 1 pixel, IPL/INL errors -0.02 pixels and OPL/INL errors 0.03 pixels were approximate to zero, NFL/GCL errors 0.74 pixels was maximum error, but were respectively better than those computed between the observers. Following main steps of proposed method, Fig.6 also illustrates that the visual comparison of automatic (yellow) versus the reference standard (red) segmentation on images with organic texture and blood vessel artifacts. it is inevitable challenge for automated segmentation thickness map generation [29]. In our proposed algorithm, an affinity matrix is incorporated neighboring information during manifold ranking, and it is effectively overcome the blood vessel discontinuity problem as illustrated in Fig.6.

Fig.7 shows that the thickness differences between the proposed algorithm and the reference standard were all smaller than the axial resolution of 3.28 μm(0.81 pixel), and were also smaller than or closed to those computed between the observers.

As shown in Fig.8, respectively, we compute and plot the signed and unsigned border position differences of the main eight boundaries between the proposed algorithm and the reference standard in the dataset, when the degree N of the polynomial curve fitting is set from 4 to 32, 12 to 40, or 16 to 44. The two plots show that the signed and unsigned border positioning errors of all the fitting boundaries are only small fluctuations, namely, with increase the degree N of the polynomial curve fitting, these errors don't change. Therefore, the result plots suggest that the connected components of the most boundaries are always continuously and perfectly extracted by our proposed algorithm.

Table 1
Unsigned border position differences (mean±SD in pixel) and Signed border position differences (mean±SD in pixel) of 51 scans using our normal segmentation mode in Dataset

| Segmenter / Border	Unsigned border position differences				Signed border position differences			
	Obs.1 vs.Obs.2	Algo_Prop osed. vs. Obs.1	Algo_Pro posed.vs. Obs.2	Alo_Pro posed. vs. Avg.Obs.	Obs.1 vs.Obs.2	Algo_Prop osed. vs. Obs.1	Algo_Pro posed.vs. Obs.2	Alo_Pro posed. vs. Avg.Obs.
ILM	1.24±0.34	0.76±0.20	0.95±0.20	0.66±0.13	1.01±0.47	-0.37±0.36	0.64±0.29	0.13±0.23
NFL/GCL	1.62±0.42	1.81±0.49	1.14±0.30	1.27±0.34	-1.15±0.56	1.31±0.66	0.16±0.49	0.74±0.51
IPL/INL	1.46±0.39	1.36±0.27	0.97±0.19	0.94±0.18	-1.05±0.59	1.15±0.47	0.10±0.41	0.62±0.33
INL/OPL	1.38±0.30	1.18±0.28	1.05±0.28	0.91±0.22	0.05±0.63	-0.04±0.49	0.01±0.44	-0.02±0.34
OPL/INL	1.84±0.56	1.57±0.43	1.42±0.55	1.19±0.39	-1.15±0.91	0.60±0.78	-0.54±0.76	0.03±0.62
ELM	1.19±0.44	0.75±0.25	1.19±0.44	0.84±0.28	0.60±0.61	-0.43±0.64	0.16±0.74	-0.14±0.62
IS/CL	1.19±0.29	0.54±0.18	0.95±0.23	0.55±0.13	0.91±0.48	-0.22±0.30	0.69±0.34	0.23±0.21
BM/Choroid	1.43±0.46	1.54±1.20	1.07±1.05	1.11±1.12	-1.23±0.56	1.43±1.27	0.19±1.23	0.81±1.22
Overall	1.42±0.09	1.19±0.34	1.09±0.29	0.94±0.32	-0.25±0.14	0.43±0.31	0.18±0.31	0.30±0.33
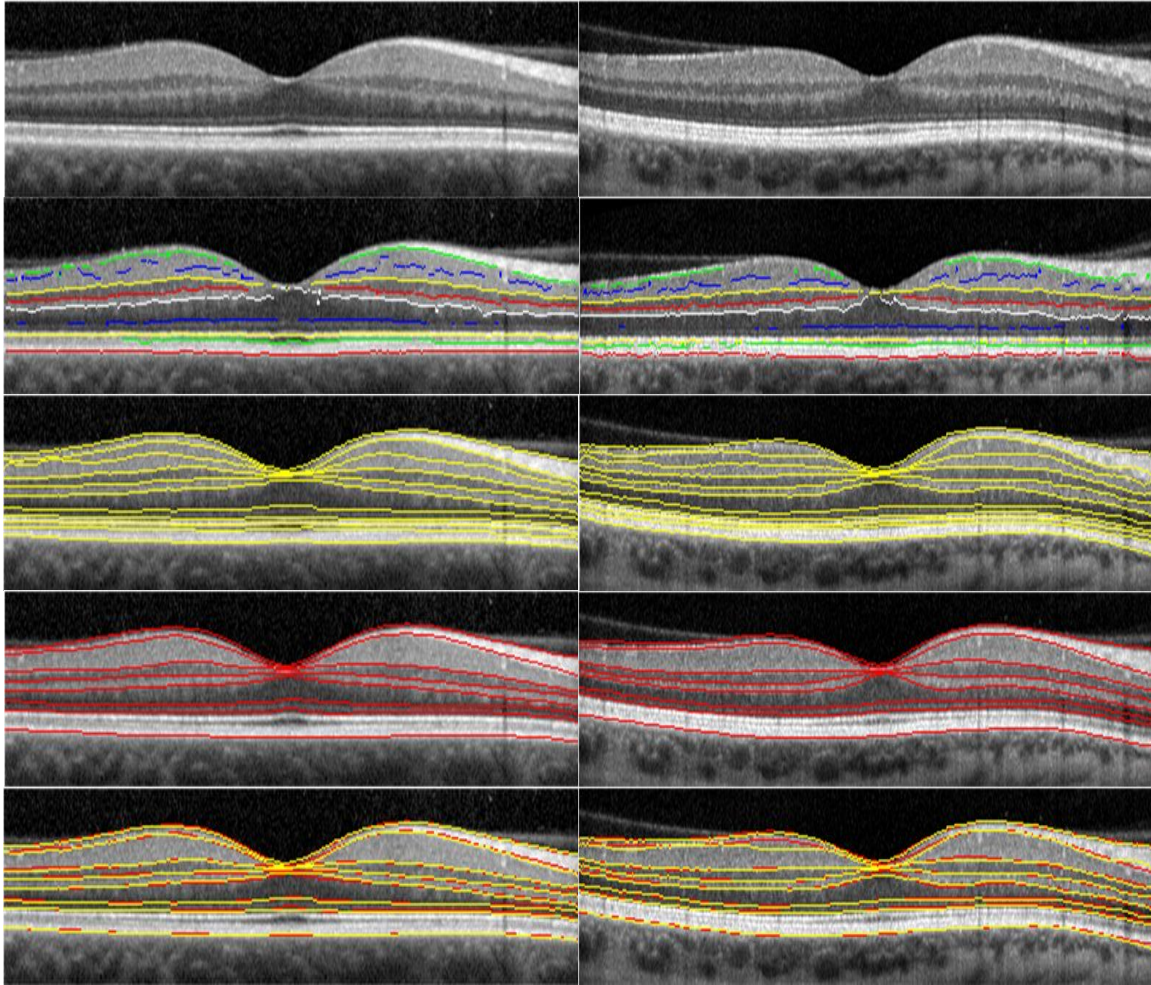
Fig. 6. Comparison of automatic (yellow) versus the reference standard (red) segmentation on images with organic texture artifacts and blood vessel artifacts. (row a) Original image.(row b) Detected the connected components with our proposed automatic method. (row c) Final segmentation with our proposed automatic method after smoothing. (row d) Final segmentation with the reference standard. (row e) Comparison of automatic (yellow) versus the reference standard (red).
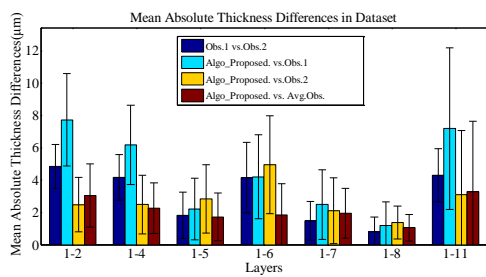

Fig.7. Bar charts show mean thicknesses differences of the main intra-retinal layers in dataset.
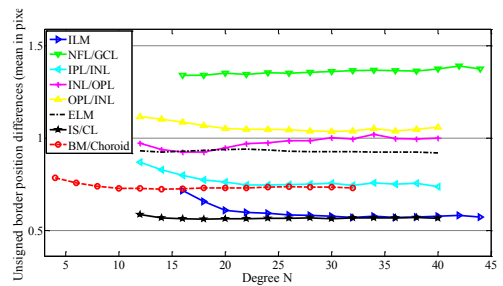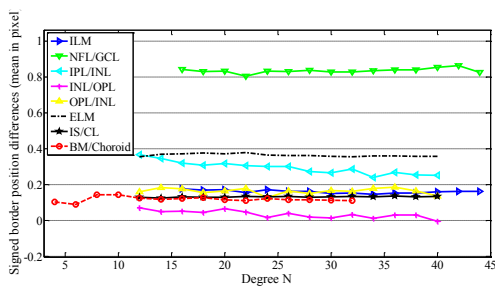
Fig.8. The error result plots show the border position differences of the main eight boundaries between the proposed algorithm and the reference standard in dataset, when the degree N of the polynomial curve fitting is set from 4 to 32, 12 to 40, or 16 to 44. Up: the signed border position differences. Down: the unsigned border position differences.

Fig.9 illustrates a segmentation result robustness in OCT image for the age related macular degeneration, and shows the detected boundaries accurately track all the eleven boundaries by our proposed algorithm, superpixels and connected components can effectively overcome the boundaries discontinuity problem as illustrated in Fig.9.

(a)

(b)

(c)

(d)

(e)

(f)

(g)
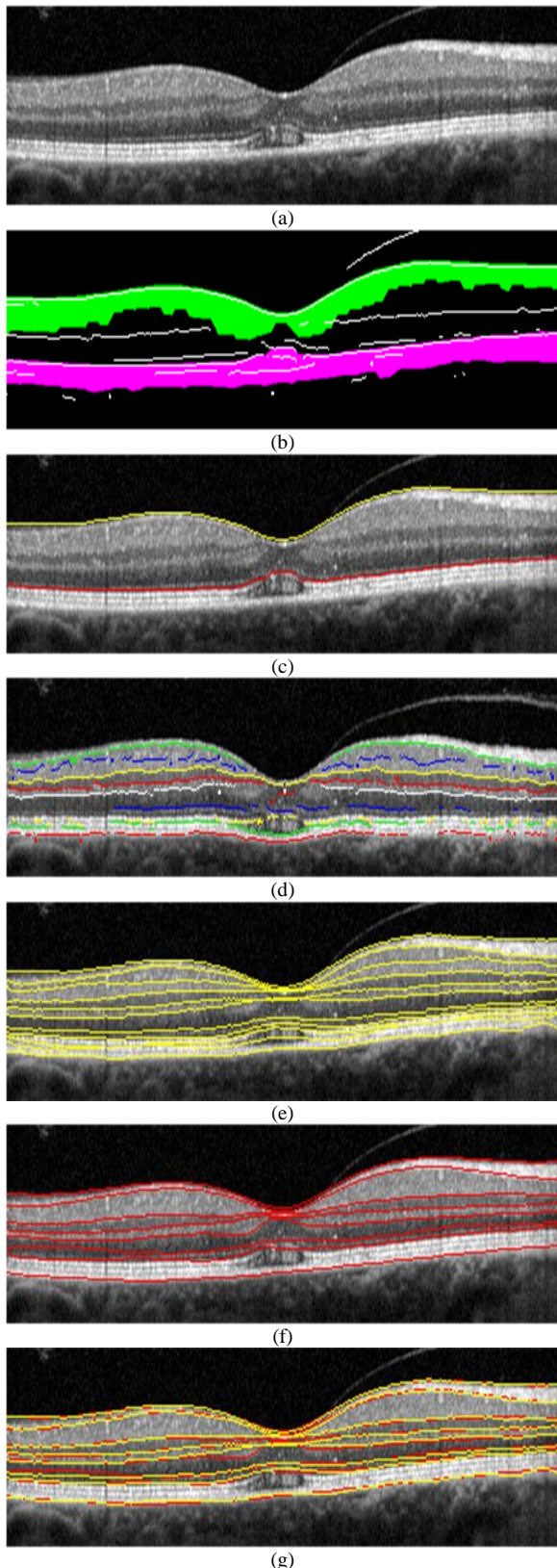
Fig.9. Comparison of automatic (yellow) versus manual (red) segmentation on image for the age related macular degeneration. (a) Original image. (b)Fusion image by the segmented superpixels and the main connected components around the ILM and IS/CL boundaries (c) Result of the ILM and IS/CL boundaries after smoothing. (d) Detected the connected components with our proposed automatic method (e) Original image with computer-segmented borders. (f) Original image showing reference standard.

(g) Comparison of computer-segmentation (yellow) and reference standard (red).

4. **Conclusion**

This paper proposes a graph-based SLIC superpixels and manifold ranking method to segment macular retinal layers in OCT images. we considers the superpixels and connected components as nodes, which incorporates gradient cues and spatial priors of the connected components. Based on the gradient sum and spatial distance of the connected components, we utilize a three-stage graph-based Dijkstra's method and manifold ranking approach to extract corresponding boundaries. We evaluate the proposed algorithm on main boundaries error and layers thickness error. It demonstrates promising results with comparisons to the manual tracings of two independent observers. Furthermore, like super-pixel method, the proposed algorithm is computationally efficient, and is not relatively susceptible to speckle noise or artifacts. The future work will focus on segmentation of retinal layers in OCT images with applications to ocular disease problems.

Acknowledgement

References

[1]   D. Huang, E. A. Swanson, C. P. Lin, J. S. Schuman, W. G. Stinson, W. Chang, M. R. Hee, T. Flotte, K. Gregory, C. A. Puliafito, and J. G. Fujimoto, "Optical coherence tomography, " Science 254(1991), 1178–1181.

[2]   M. Wang, D. C. Hood, J. S. Cho, Q. Ghadiali, G. V. De Moraes, X. Zhang, R. Ritch, and J. M. Liebmann, "Measurement of local retinal ganglion cell layer thickness in patients with glaucoma using frequency-domain optical coherence tomography," Arch. Ophthalmol. 127(2009), 875–881.

[3]   H. W. van Dijk, P. H. Kok, M. Garvin, M. Sonka, J. H. Devries, R. P. Michels, M. E. van Velthoven, R. O. Schlingemann, F. D. Verbraak, and M. D. Abràmoff, "Selective loss of inner retinal layer thickness in type 1 diabetic patients with minimal diabetic retinopathy," Invest. Ophthalmol. Vis. Sci. 50(2009), 3404–3409.

[4]   D. Cabrera DeBuc, and G. M. Somfai, "Early detection of retinal thickness changes in diabetes using Optical Coherence Tomography," Med. Sci. Monit 16(2010), 15–21.

[5]   Q.Zhao, X. Qian, L. Li, "Effect of elevated intraocular pressure on the thickness changes of cat laminar and prelaminar tissue using optical coherence tomography," Bio-Medical Materials and Engineering 24 (2014), 2349-2360.

[6]   J. F. de Boer, B. Cense, B. H. Park, M. C. Pierce, G. J. Tearney, and B. E. Bouma, "Improved signal-to-noise ratio

in spectral-domain compared with time-domain optical coherence tomography, " Opt. Lett.28(2003), 2067–2069.

[7] D. Koozekanani, K. Boyer, and C. Roberts, "Retinal thickness measurements from optical coherence tomography using a Markov boundary model," IEEE Trans. Med. Imag.20(2001), 900–916.

[8] D. C. Fern´andez, H. M. Salinas, and C. A. Puliafito, "Automated detection of retinal layer structures on optical coherence tomography images," Opt.Exp. 13(2005),10200–10216.

[9] M. Mujat, R. Chan, B. Cense, B. Park, C. Joo, T. Akkin, T. Chen, and J. de Boer, "Retinal nerve fiber layer thickness map determined from optical coherence tomography images," Opt. Express 13 (2005), 9480–9491.

[10] A. Mishra, A. Wong, K. Bizheva, and D. A. Clausi, "Intra-retinal layer segmentation in optical coherence tomography images," Opt. Exp.17(2009)23719–23728.

[11] MA. Mayer, R. P. Tornow, R. Bock, J. Hornegger and F. E. Kruse, "Automatic Nerve Fiber Layer Segmentation and Geometry Correction on Spectral Domain OCT Images Using Fuzzy C-Means Clustering," Invest. Ophthalmol. Vis. Sci. 49(2008), 1880.

[12] V. Kaji´c, B. Pova˘zay, B. Hermann, B. Hofer, D. Marshall, P. L. Rosin, and W. Drexler, "Robust segmentation of intraretinal layers in the normal human fovea using a novel statistical model based on texture and shape analysis," Opt. Exp.18(2010)14730–14744.

[13] K. A. Vermeer, J. van der Schoot, H. G. Lemij, and J. F. de Boer, "Automated segmentation by pixel classification of retinal layers in ophthalmic OCT images," Biomed. Opt. Exp., 2(2011)1743–1756.

[14] M.K. Garvin, M.D. Abramoff, "Automated 3-D Intraretinal Layer Segmentation of Macular pectral-Domain Optical Coherence Tomography Images," IEEE Transaction on Medical Imaging, 28(2009), 1436–1447.

[15] Q. Yang, CA. Reisman, Z. Wang, Y. Fukuma, M. Hangai, N. Yoshimura, A. Tomidokoro, M. Araie, AR. Raza, DC. Hood and K. Chan, "Automated layer segmentation of macular OCT images using dual-scale gradient information," Optics Express. 18(2010), 21294-21307.

[16] SJ. Chiu, XT .Li, P. Nicholas, CA. Toth, JA. Izatt, and S. Farsiu, "Automatic segmentation of seven retinal layers in SDOCT images congruent with expert manual segmentation, " Optic Express, 18(2010), 19413-19428.

[17] R Kafieh, H Rabbani, MD Abramoff, M Sonka, "Intra-retinal layer segmentation of 3D optical coherence tomography using coarse grained diffusion map, Medical image analysis," 17(2013), 907–928.

[18] R Kafieh, H Rabbani, F Hajizadeh, MD. Abramoff, and M Sonka, "Thickness Mapping of Eleven Retinal Layers Segmented Using the Diffusion Maps Method in Normal Eyes," Journal of Ophthalmology, vol. 2015, Article ID 259123, 14 pages, 2015. doi:10.1155/2015/259123.

[19] Y. M. Cha, J.H. Han, "High-Accuracy Retinal Layer Segmentation for Optical Coherence Tomography Using Tracking Kernels Based on Gaussian Mixture Model," IEEE Journal of Selected Topics in Quantum Electronics, 20(2014),1743–1756.

[20] Fei Shi, Xinjian Chen, Heming Zhao, Weifang Zhu, Dehui Xiang, Enting Gao, Sonka, M., Haoyu Chen. Automated 3-D Retinal Layer Segmentation of Macular Optical Coherence Tomography Images With Serous Pigment Epithelial Detachments, IEEE Trans Medical Imaging, 2015: 34(2): 441 - 452.

[21] Achanta, R, Shaji, A, Smith, K, Lucchi, A, Fua, P, Süsstrunk, S. SLIC Superpixels Compared to State-of-the-Art Superpixel Methods. IEEE Trans Pattern Analysis and Machine Intelligence 2012;34(11) : 2274 - 2282.

[22] Trulls E, Tsogkas S, Kokkinos I, Sanfeliu A, Moreno-Noguer F. Segmentation-Aware Deformable Part Models, IEEE International Conference of Computer Vision and Pattern Recognition (CVPR), 2014.p.168 - 175.

[23] D. Zhou, J. Weston, A. Gretton, O. Bousquet, and B. Scholkopf, "Ranking on data manifolds," In NIPS, 2004. 2, 3

[24] B. Scholkopf, J. Platt, J. Shawe-Taylor, A. Smola, and R. Williamson, "Estimating the support of a high-dimensional distribution," Neural Computation, 2001. 3

[25] S. Brin and L. Page, "The anatomy of a large-scale hypertextual web search engine," Computer networks and ISDN systems, 30(1):107–117, 1998. 2

[26] A. Ng, M. Jordan, Y. Weiss, et al, "On spectral clustering: Analysis and an algorithm," In NIPS, pages 849–856, 2002.

[27] C. Yang and L.H.Zhang, H. C. Lu, et al, "Saliency Detection via Graph-Based Manifold Ranking," In CVPR, 2013. 1

[28] Canny, John, "A Computational Approach to Edge Detection," IEEE Transactions on Pattern Analysis and Machine Intelligence, 8(1986), 679-698.

[29] D. C. Hood, B. Fortune, S. N. Arthur, D. Xing, J. A. Salant, R. Ritch, and J. M. Liebmann, "Blood vessel contributions to retinal nerve fiber layer thickness profiles measured with optical coherence tomography," J. Glaucoma 17(7), 519–528 (2008).